CJC Chinese Journal of Chemistry 中国化学 - An International Journal

For submission: https://mc.manuscriptcentral.com/cjoc
For published articles: https://onlinelibrary.wiley.com/journal/16147065

Concise Report

Cite this paper: *Chin. J. Chem.* **2024**, *42*, 3075—3082. **DOI: 10.1002/cjoc.202400573**

Small-Molecular Donor Based Efficient Organic Solar Cells with Thermally Stable Morphologies†

Wanying Feng,[‡,a,b] Yuyang Bai,[‡,a] Jiaying Wang,[a] Shaohui Yuan,[a] Xiangjian Wan,[b] Yu Chen,[c] Bin Kan,*[,a] and Yongsheng Chen[b]

[a] *School of Materials Science and Engineering, National Institute for Advanced Materials, Nankai University, Tianjin 300350, China*
[b] *State Key Laboratory and Institute of Elemento-Organic Chemistry, Frontiers Science Center for New Organic Matter, The Centre of Nanoscale Science and Technology and Key Laboratory of Functional Polymer Materials, Renewable Energy Conversion and Storage Center (RECAST), College of Chemistry, Nankai University, Tianjin 300071, China*
[c] *Beijing Synchrotron Radiation Facility, Institute of High Energy Physics, Chinese Academy of Sciences, Beijing 100043, China*

Keywords

Organic solar cells | Small-molecular donor | Small-molecular acceptor | Dimeric acceptor | Morphological thermal stability

Comprehensive Summary

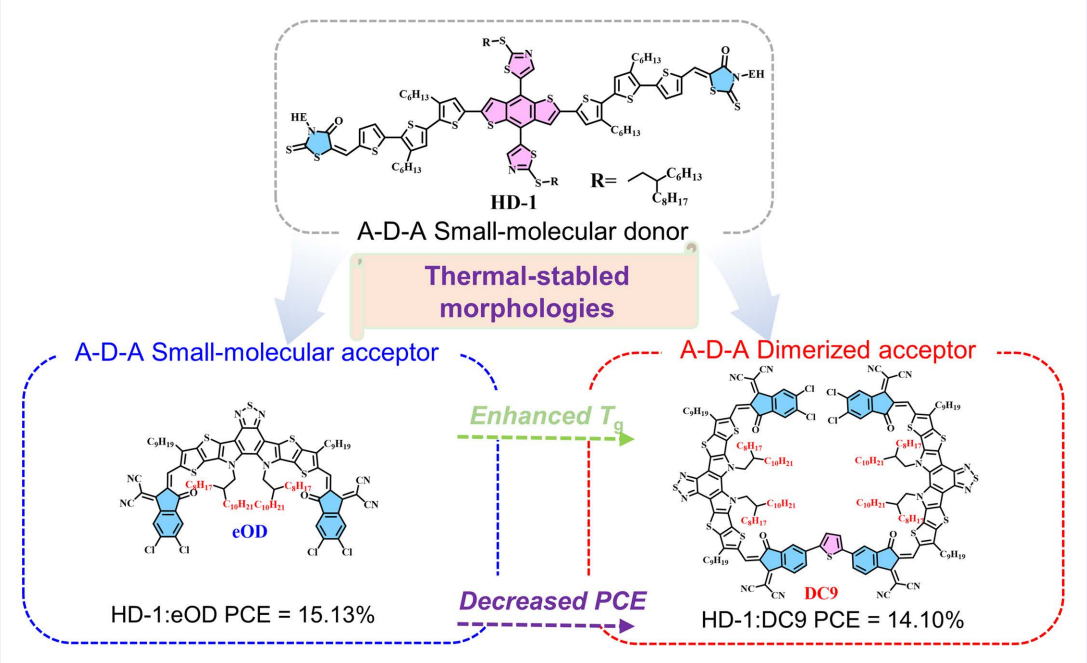

Small-molecular organic solar cells usually exhibited unsatisfactory device stability, which might originate from their molecular diffusion behaviors. Herein, based on the all-small-molecule system HD-1:BTP-eC9, we reported a dimerized acceptor DC9, and its corresponding monomer acceptor eOD. In comparison with eOD, the dimeric acceptor DC9 displayed higher glass transition temperature (T_g) but reduced molecular planarity and crystallinity. The all-small molecule blend utilizing HD-1:eOD demonstrated a power conversion efficiency (PCE) of 15.13%, surpassing the value of 14.10% for the HD-1:DC9 blend. While, incorporating polymer donor PM6 into the HD-1:DC9 blend improved its morphology and charge transport dynamics, resulting in a device efficiency of over 16%, representing the rare case utilizing small-molecular donor and dimeric acceptor with PCE over 16%. Morphological characterization results affirmed that the surface morphologies and molecular packing behaviors of the blend films based on HD-1 were largely retained even after prolonged annealing and aging at 85 °C. Consequently, the PCEs of the blend films based on HD-1:eOD, HD-1:DC9, and HD-1:PM6:DC9 consistently remained over 98% of their initial efficiency after 1000 h of thermal annealing aging at 85 °C. These findings highlight the potential of small-molecular based active layer in the fabrication of efficient and stable OSCs.

*E-mail: kanbin04@nankai.edu.cn
[‡] These authors contributed equally.
[†] Dedicated to the Special Issue of Emerging Investigators in 2024.

Background and Originality Content

All-small-molecule organic solar cells (ASM-OSCs) further improve the advantages of organic small-molecule photovoltaic materials, including their well-defined chemical structures, minimal batch-to-batch variations, and easily tunable properties.[1] Furthermore, unlike polymer-based OSCs, ASM-OSCs provide a crucial platform for investigating the relationships between the chemical structures of materials and their versatile properties; thus, prompting the development of new materials.[2] Remarkably, the recent emergence of Y-series non-fullerene acceptors (Y-NFAs)[3] and the successful development of acceptor–donor–acceptor (A–D–A)-structured small-molecule donors (SMDs)[4] has facilitated the realization of enhanced photon utilization efficiencies and reduced energy losses, significantly enhancing the power conversion efficiencies (PCEs) of ASM-OSCs to over 17%.[5] However, despite these improvements in the PCEs of ASM-OSCs, their long-term stabilities need to be enhanced to facilitate practical applications.[6]

Accordingly, various strategies based on material innovation and device optimization have been introduced to improve the stabilities of ASM-OSCs. For instance, Badgujar *et al*. developed fullerene-free ASM-OSCs using BDT3TR and the small-molecule acceptor O-IDTBR, achieving superior PCEs and considerably better thermal stabilities compared to BDT3TR:$PC_{71}BM$ devices.[7] Furthermore, Gao *et al.* integrated the layer-by-layer deposition approach and methoxy-substituted graphdiyne solid additive treatment to manipulate active layer morphology and improve device stability.[5b] Meanwhile, Min *et al*. implemented a two-step solvent treatment approach to fabricate high-performance ASM-OSCs without interfacial layers, achieving improved device stabilities.[8] Despite these notable advancements, the factors responsible for the instabilities of ASM-OSCs continue to be debated, and comprehensive stability studies on ASM-OSCs are limited. Under these circumstances, dimerized NFAs (DMAs) based on Y-series molecules with high glass transition temperatures (T_g) and delicate molecular structures have garnered particular attention. Remarkably, compared to other types of NFAs, these DMAs demonstrate enhanced device stabilities, along with significantly higher PCEs.[9] However, the potential synergy between SMDs and DMAs during OSC fabrication remains largely unexplored, prompting further investigations into the ability of this combination to enhance the thermal stabilities of high-performance SMD-based devices.

Leveraging the efficient ASM system HD-1:BTP-eC9, this study designed and synthesized a dimerized acceptor, DC9, and its corresponding monomer acceptor, eOD.[5a] Following device optimization, HD-1:eOD, and HD-1:DC9 afforded PCEs of 15.13% and 14.10%, respectively. Moreover, the introduction of PM6 as the third component in the HD-1:DC9 active layer led to morphological improvements and PCE enhancements to 16.03%, comparable to the PCEs of high-efficiency ASM-OSCs. Notably, this study pioneers the application of SMD:DMA blends in the fabrication of OSCs, setting new performance benchmarks for SMD:DMA-based OSCs. Importantly, all HD-1-based blend films demonstrated consistent absorption characteristics, surface morphologies, and molecular stacking behaviors even after annealing at 85 °C for 1000 h, maintaining over 98% of their initial PCEs. These findings underscore the applicability of active layer materials with well-defined molecular structures and thermally stable morphological features in the fabrication of efficient and stable ASM-OSCs.

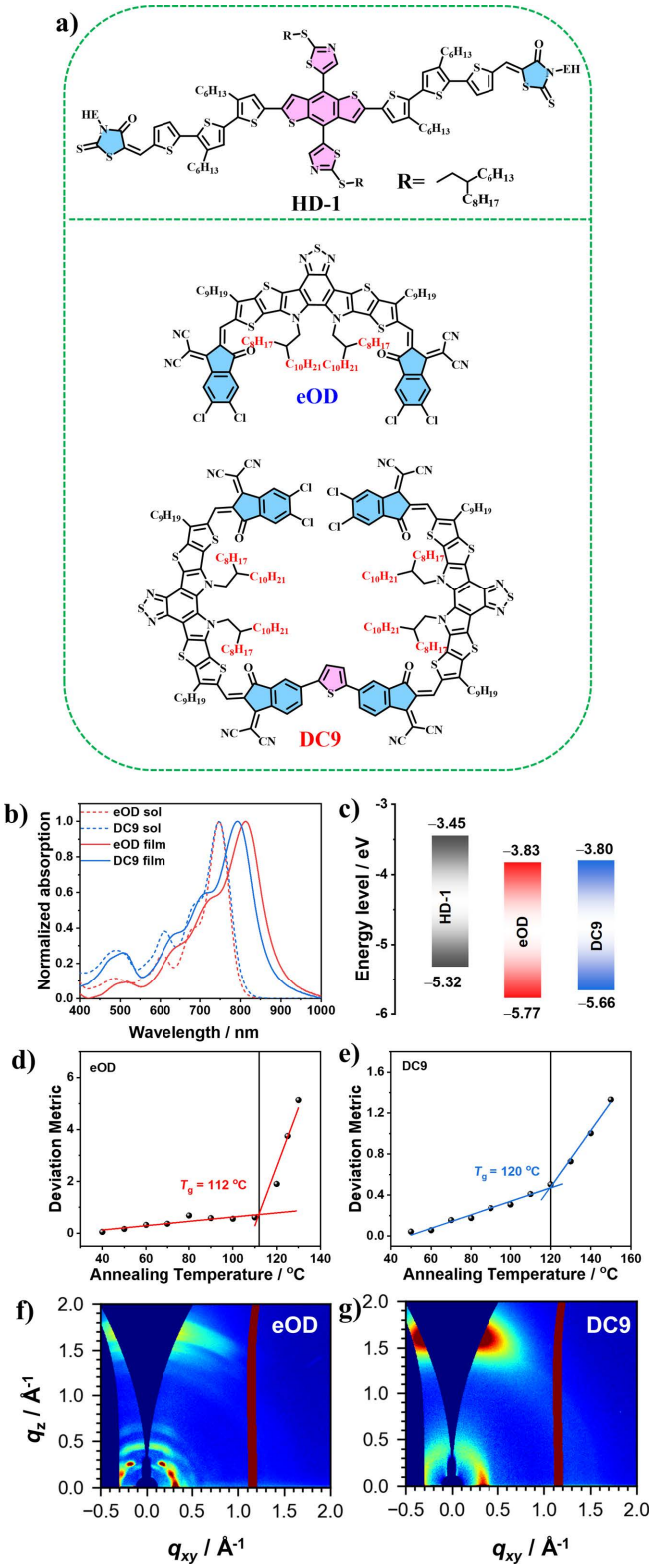

Figure 1 a) Chemical structures of HD-1, eOD, and DC9, respectively; b) Normalized absorption spectra of eOD and DC9 in their diluted solutions and thin-film states; c) Diagram of energy levels of HD-1, eOD, and DC9; Estimation of T_g for d) eOD, and f) DC9, respectively; 2D GIWAXS patterns of f) eOD thin film, and g) DC9 thin film, respectively.

Results and Discussion

Material synthesis and properties

Figure 1a displays the chemical structures of the SMD HD-1, small-molecule acceptor eOD, and dimeric acceptor DC9. Among these, HD-1, featuring an A–D–A-conjugated backbone, is a highly efficient electron donor recently developed by our group, while eOD was synthesized according to the methodology of a previous study. By combining two eOD units based on the end-to-end strategy, the dimeric molecule DC9 was successfully synthesized in reasonably high yields through typical organic reactions. Scheme

S1 depicts the synthetic pathways for eOD and DC9, while additional details, including nuclear magnetic resonance spectra, are available in the Supporting Information. Generally, owing to elongated alkyl chains (2-octyldodecyl) on their pyrrole units, both the monomer eOD and dimer DC9 demonstrate high solubilities in common organic solvents, facilitating their solution-processability in device fabrication.

Following these optical-property assessments, we investigated the differences in the electrochemical properties of eOD and DC9 in the thin-film states through cyclic voltammetry (CV) measurements. Subsequently, the highest occupied molecular orbital (HOMO) and lowest unoccupied molecular orbital (LUMO) energy levels were computed based on the oxidation and reduction potentials derived from the CV curves (Figure S1), respectively. Figure 1c displays the energy level alignments of eOD, DC9, and HD-1. Notably, the HOMO and LUMO energy levels of eOD were obtained as −5.77 eV and −3.83 eV (Table 1), respectively. Upon connecting two eOD analogues in an end-to-end manner with a thiophene linker, the HOMO and LUMO energy levels of DC9 slightly increased to −5.66 eV and −3.80 eV, respectively. This subtle elevation in the LUMO level of DC9 compared to that of eOD may yield higher open-circuit voltages (V_{OC}) in OSCs. Additionally, the HOMO and LUMO energy offsets (ΔHOMO and ΔLUMO) between the electron donor (HD-1) and electron acceptor (eOD or DC9) exceeded 0.30 eV, providing a strong driving force for charge separation in the HD-1:eOD and HD-1:DC9 blend films.[10]

Table 1 Summary of properties of HD-1, eOD and DC9

Comp.	$\lambda_{max}^{sol.}$/nm	λ_{max}^{film}/nm	λ_{onset}/nm	E_g^{opt}/eV	LUMO/eV	HOMO/eV
HD-1	518	582/631	719	1.72	−3.45	−5.32
eOD	746	812	896	1.38	−3.83	−5.77
DC9	746	793	870	1.43	−3.80	−5.66

Notably, one of the motivations of constructing dimer materials is the development of novel materials with T_g, which could help to suppress the molecular diffusion and enhance device stability in OSCs under long-term operation.[11] As depicted in Figure 1d, 112 °C and 120 °C were determined as the T_g values of eOD and DC9 under the thin-film state based on UV–Vis measurements, respectively. Notably, although the increased molecular weight of DC9 contributes to its higher T_g, it also leads to reduced molecular crystallinity and inhibited stacking behaviors, as evidenced by the grazing incidence wide-angle X-ray diffraction (GIWAXS) results. As illustrated in Figure 1e, the diffraction profile of the DC9 thin film presented a single (010) π–π diffraction peak along the out-of-plane (OOP) direction, alongside (100) alkyl-to-alkyl diffraction peak along the in-plane (IP) direction. Conversely, the diffraction profile of the eOD thin film presented multiple high-order diffraction signals along the OOP direction, suggesting enhanced long-range molecular order and higher crystallinity of eOD in the solid state. Analyses of the π–π diffraction signal along the OOP direction revealed that the p-p stacking distance ($d_{p\text{-}p}$) and correlated coherence length (CL) of eOD were 3.76 Å and 25.9 Å (Figure S2 and Table S1), respectively, whereas for DC9, the $d_{\pi-\pi}$ and CL values were 3.97 Å and 17.3 Å, respectively. Furthermore, the CL of the alkyl-to-alkyl region in the DC9 thin film was determined to be 50.2 Å, significantly shorter than the corresponding length of 106 Å, evident in the eOD film. Collectively, these findings suggest poor molecular stacking in the dimeric DC9 thin film compared to that in monomeric eOD.

To elucidate the factors responsible for the differing molecular packing motifs observed between eOD and DC9, their molecular conformations were computed and optimized based on density functional theory calculations at the B3LYP/6-31G* level. As depicted in Figure S3, the conjugated skeletons of eOD appeared nearly co-planar, demonstrating its excellent molecular planarity. In contrast, the dimeric molecule DC9 featured a large dihedral angle of approximately 35° between its two planar eOD wings. This angle likely contributes to the poor intermolecular packing behaviors of DC9, as mentioned previously.

Photovoltaic and charge dynamic properties

Based on the findings of the foregoing analyses, solution-processed OSCs were fabricated employing the conventional ITO/PEDOT:PSS/active layer/PDINO/Ag device architecture to assess the photovoltaic performance of eOD and DC9 when blended with the SMD HD-1. The preparation conditions for the HD-1:eOD and HD-1:DC9 active layers are detailed in the Supporting Information. Figure 2a depicts the *J*–V curves of the optimal devices, while Table 2 summarizes photovoltaic parameters. Notably, the ASM-OSC incorporating HD-1:eOD achieved a PCE of 15.13%, with a V_{OC} value of 0.865 V, a J_{SC} value of 23.41 mA·cm^{-2}, and a fill factor (*FF*) of 74.75%. In contrast, the ASM-OSC incorporating HD-1:DC9 exhibited an improved V_{OC} value exceeding 0.90 V; however, its reduced J_{SC} and *FF* values of 22.59 mA·cm^{-2} and 68.99%, respectively, led to an overall PCE of 14.10%. To the best of our knowledge, this study represents one of the few instances of combining an SMD with a dimeric acceptor, thus paving the way for future advancements in SMD-based OSCs. To further enhance the performance of the HD-1:DC9 blend, the conjugated polymer donor PM6 was introduced as the third component. Upon optimizing the addition ratio of PM6 (Table S2), simultaneous improvements in the J_{SC} to 23.72 mA·cm^{-2} and *FF* to 75.98% contributed to a high PCE of 16.03% in OSCs based on HD-1:PM6:DC9 at a weight ratio of 7 : 3 : 7. Thus, the inclusion of PM6 not only optimized the morphological features of the blends but also created an extended pathway for charge transport, as will be discussed later.

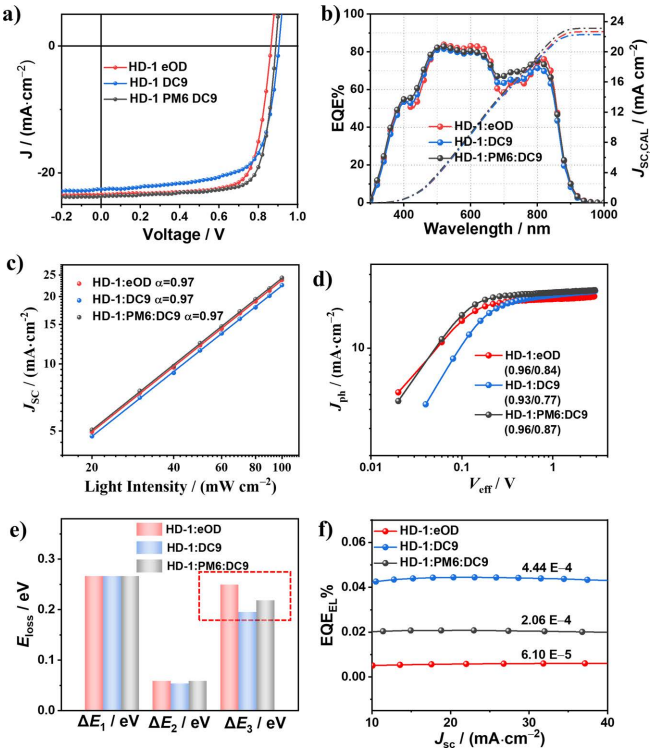

Figure 2 a) *J*-V curves, b) EQE curves, c) J_{ph} versus V_{eff}, d) light intensity dependence of J_{sc}, e) diagrams of energy losses, and f) EQE_{EL} of HD-1:eOD, HD-1:DC9, and HD-1:PM6:DC9 devices, respectively.

Notably, the distinct J_{SC} values of the HD-1:eOD, HD-1:DC9, and HD-1:PM6:DC9 blends are among the primary factors influencing the photovoltaic performance of the resulting OSCs. Thus, the J_{SC} values obtained from the *J*–V curves were further validated based on external quantum efficiency (EQE) measurements. All

devices incorporating the HD-1:eOD, HD-1:DC9, and HD-1:PM6:DC9 blends presented similar EQE response ranges extending up to 900 nm. However, their distinct EQE values resulted in integrated J_{SC} values ($J_{SC,CAL}$) of 22.68, 22.27, and 23.41 mA·cm^{-2}, respectively. Notably, these $J_{SC,CAL}$ values demonstrate less than 3% discrepancies compared to the J_{SC} values derived from the *J*–V curves, confirming the reliability of our measurements. As depicted in Figure 2b, compared to both the HD-1:DC9- and HD-1:PM6:DC9-based devices, the HD-1:eOD-based device exhibited enhanced EQE responses in the donor-dominated spectral region extending from 500—650 nm. This indicates more efficient photoelectrical conversion processes between the donor and acceptor in the HD-1:eOD blend. Notably, the inclusion of PM6 in the HD-1:DC9 blend primarily enhanced the EQE responses in the acceptor-dominated region extending from 650—850 nm, resulting in an enhancement of ~1 mA·cm^{-2} in its J_{SC} value compared to that for the HD-1:DC9-based device.

Table 2 Photovoltaic parameters of HD-1:eOD, HD-1:DC9, and HD-1:PM6:DC9 devices. Average values with standard deviations obtained from 15 devices.

Active Layer	V_{OC}/V	J_{SC}/(mA·cm^{-2})	*FF*/%	PCE[a]/%
HD-1:eOD	0.865 (0.864±0.002)	23.41 (23.29±0.16)	74.75 (74.45±0.42)	15.13 (14.98±0.15)
HD-1:DC9	0.905 (0.905±0.001)	22.59 (22.27±0.20)	68.99 (68.31±0.78)	14.10 (13.76±0.17)
HD-1:PM6:DC9	0.889 (0.886±0.003)	23.72 (23.47±0.16)	75.98 (75.61±0.50)	16.03 (15.73±0.17)

Furthermore, the distinct EQE profiles of the devices were gauged to gain insights into their charge dynamics. Specifically, the short-circuit current densities (J_{SC}) of the devices under varying incident light intensities (P_{in}) and their photocurrent densities (J_{Ph}) at the effective voltage (V_{eff}) were recorded, and the relationship between J_{SC} and P_{in} was analyzed based on $J_{SC} \propto P_{in}^{\alpha}$, where α serves as an indicator of bimolecular recombination within the device.[12] After fitting the curves, as depicted in Figure 2c, identical α value of 0.97 was obtained for all three devices, indicating similar but lower levels of bimolecular recombination across all devices. Furthermore, as depicted in Figure 2d, when the effective voltage exceeded 1.5 V, the current densities of all three devices reached saturation (J_{sat}), indicating a complete collection of photogenerated charges under these conditions.[13] Subsequently, leveraging existing techniques, the exciton dissociation efficiency (P_{diss}) and charge collection efficiency (P_{coll}) of the HD-1:eOD-based device were estimated to be 0.96 and 0.84, respectively. However, for the HD-1:DC9-based device, these values decreased to 0.93 and 0.77, respectively, correlating with its suboptimal J_{SC} and *FF* values. Furthermore, after replacing a portion of HD-1 with PM6, the charge collection efficiency of the device significantly increased, achieving the highest P_{coll} value of 0.87 among all three devices. This excellent P_{coll} value of the HD-1:PM6:DC9-based device, combined with its superior exciton dissociation (P_{diss} is 0.96), led to its improved J_{SC} and *FF* values.

The performance of the three blends also appears to be correlated with their V_{OC} values, which present a 40 mV difference between the HD-1:eOD- and HD-1:DC9-based devices. To validate these observations, an energy loss analysis based on the detailed balance theory was conducted.[14] Fourier transform photocurrent spectroscopy–EQE (FTPS-EQE) spectra revealed an optical bandgap (E_gs) of approximately 1.43 eV for all the three blends (Figure S4).[15] Consequently, based on $E_{loss} = E_g - qV_{OC}$, the following total energy losses (E_{loss}) were derived: 0.567 eV for the HD-1:eOD-based, 0.526 eV for the HD-1:DC9-based, and 0.544 eV for the HD-1:PM6:DC9-based devices. Notably, the E_{loss} value of the HD-1:DC9-based device is 41 meV lower than that of the HD-1:eOD-based device, aligning with the difference in their V_{OC} values. Moreover, further analysis of radiative and nonradiative recombination in the three devices revealed that the nonradiative recombination loss (ΔE_3) significantly influenced the E_{loss} values of the devices (Figure 2e and Table S3). Particularly, the ΔE_3 value for the HD-1:DC9-based device was only 0.207 eV, much smaller than the corresponding value of 0.243 eV for the HD-1:eOD-based device. Furthermore, to better evaluate the ΔE_3 values of the three devices, their electroluminescence quantum efficiencies (EQE_{EL}) were measured.[16] As depicted in Figure 2f, the HD-1:DC9-based device yielded the highest EQE_{EL} value of 4.44 × 10^{-4} among the three devices. Notably, this value not only contributes to its smallest ΔE_3 value but also demonstrates the potential of dimeric acceptors in suppressing nonradiative recombination losses in OSCs.

Morphological characterizations

To comprehend the observed variations in device performance, the surface morphologies of the active layers were examined using atomic force microscopy (AFM). As depicted in Figure 3a, the HD-1:eOD, HD-1:DC9, and HD-1:PM6:DC9 blend films exhibited smooth surfaces with root mean square roughness values of 1.07, 1.12, and 1.08 nm, respectively. Notably, the HD-1:PM6:DC9 ternary blend film displayed an interpenetrating network morphology, featuring distinct nanofibers. This suggests that the inclusion of the polymer donor PM6 could optimize the morphologies of HD-1-based films while facilitating the formation of continuous charge transport pathways, leading to improved *FF* and J_{SC} values of the corresponding devices.

Following this, the molecular stacking patterns within the blend films were assessed based on the GIWAXS method.[17] Figures 3b—3c display the resulting two-dimensional diffraction images and line-cut profiles, while Table S4 presents relevant detailed parameters. Notably, all three blend films displayed evident (010) diffraction peaks along the OOP direction and (100) diffraction peaks along the IP direction, indicating a preference for face-on molecular orientations. Subsequently, the molecular stacking and crystallinity patterns within the films were evaluated considering the (010) and (100) peaks along the OOP and IP directions, as illustrated in Figures 3d—3e, respectively. Both the HD-1:eOD and HD-1:DC9 blend films exhibited a similar $d_{p\text{-}p}$ value of 3.69 Å; however, the HD-1:DC9 blend film presented a reduced CL of 24.1 Å. Additionally, the (100) stacking distance (d_{100}) in the HD-1:DC9 blend film was 23.3 Å, slightly larger than the corresponding value of 22.9 Å for the HD-1:eOD blend film. These findings suggest that the HD-1:eOD blend film exhibited denser intermolecular packing and enhanced crystallinity behaviors, improving the charge transport properties of the devices. With the replacement of a portion of HD-1 by PM6, the HD-1:PM6:DC9 blend film presented increased $d_{\pi-\pi}$ and decreased CL values in both the (010) and (100) regions, attributed to the relatively weak crystallinity of PM6 compared to that of the SMD HD-1. Despite the overall reduced CL of the HD-1:PM6:DC9-based ternary device, its interpenetrating network morphology, as evidenced by the AFM results, could overcome these shortcomings and enable effective charge dynamics, leading to improved PCEs.

In-site absorption characterization

To identify the factors responsible for the distinct morphologies of the blends, changes in the absorption spectra of their active layers were analyzed during post thermal annealing treatment through *in-situ* absorption measurements.[18] As illustrated in Figures 4a—4b, upon thermal annealing of the HD-1:eOD blend film at 140 °C, both the donor and acceptor absorption spectra exhibited a sustained redshift and enhancement within the 0—150 s timescale. These findings suggest that under thermal stress conditions, the SMD HD-1 and acceptor eOD are more likely to diffuse and migrate owing to their smaller molecular sizes.

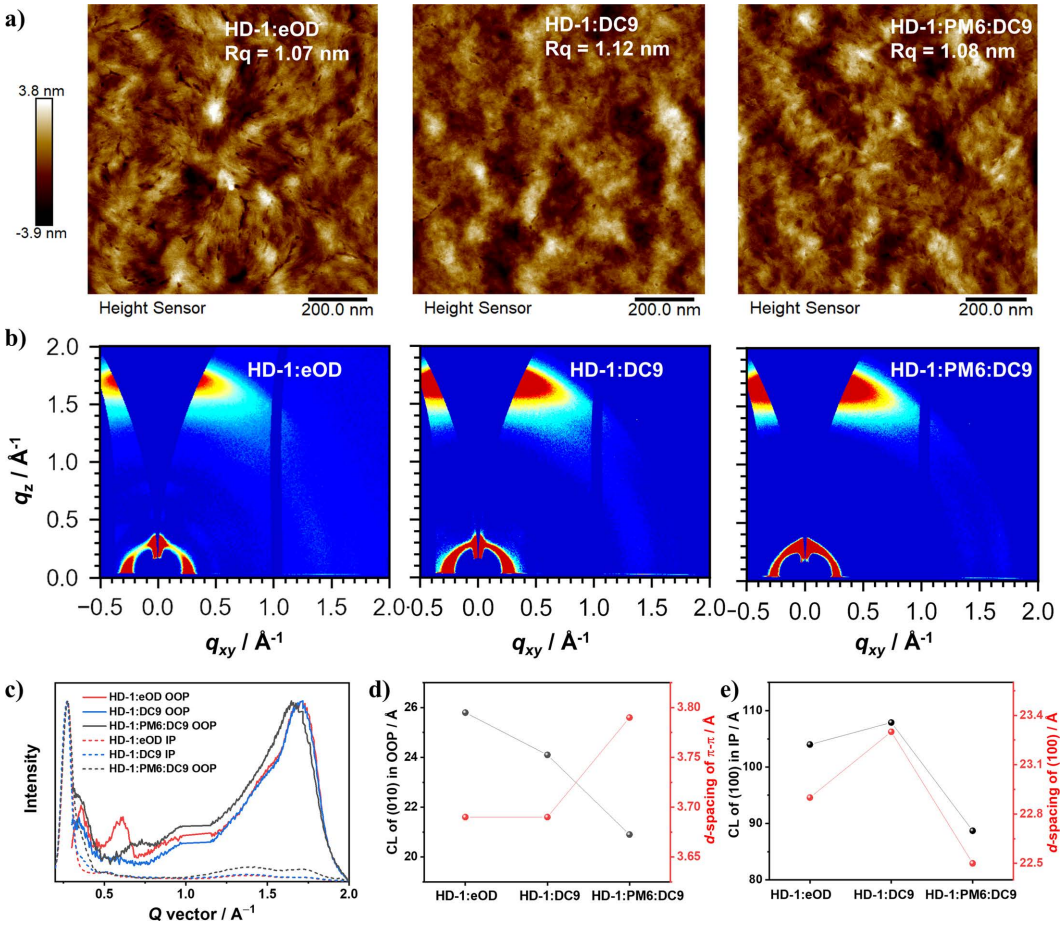

Figure 3 a) AFM images of HD-1:eOD, HD-1:DC9 and HD-1:PM6:DC9 blend films, respectively; b) GIWAXS images of HD-1:eOD, HD-1:DC9 and HD-1:PM6:DC9 blend films, respectively; c) IP and OOP line-cuts of GIWAXS results; d) π–π stacking distances and CL results in the OOP for three blend films; e) Alkyl-to-alkyl stacking distances and CL results in the IP for three blend films.

Correspondingly, the HD-1:eOD blend film exhibited a more orderly and tightly packed molecular arrangement owing to prolonged molecular motion. Conversely, as depicted in Figures 4c—4d, the absorption spectrum of the active layer (HD-1) within the HD-1:DC9 blend film presented a consistent redshift and enhancement within a relatively short timescale (0—12 s), while the absorption spectrum of DC9 remained relatively stable throughout the thermal annealing process. A similar trend was also observed in the absorption spectra of the HD-1:PM6:DC9 ternary blend film (Figures 4e—4f). These findings indicate that the larger molecular size of the dimeric acceptor DC9 limits its diffusion in the blend films under thermal stress conditions, affecting its own diffusion and that of the donor molecule and thus exerting an inhibitory effect on the molecular packing properties of the films. Thus, the processes of film formation under thermal annealing treatments influenced the molecular packing behaviors of the HD-1:eOD, HD-1:DC9, and HD-1:PM6:DC9 blend films, as corroborated by the above GIWAXS results.

Morphological thermal stability

Next, to investigate the thermal stability of the active layer morphology, blend solutions of HD-1:eOD, HD-1:DC9, and HD-1:PM6:DC9 were initially spin-coated onto ITO/PEDOT:PSS substrates, yielding corresponding films. These films were then subjected to heating and aging at 85 °C for varying durations. Following the thermal treatment, the electron transport layer was spin-coated, and the top electrode was evaporated, completing the fabrication of the devices. As mentioned previously, DC9 exhibits a higher T_g value than eOD, a characteristic often considered beneficial for morphological-stability enhancements through

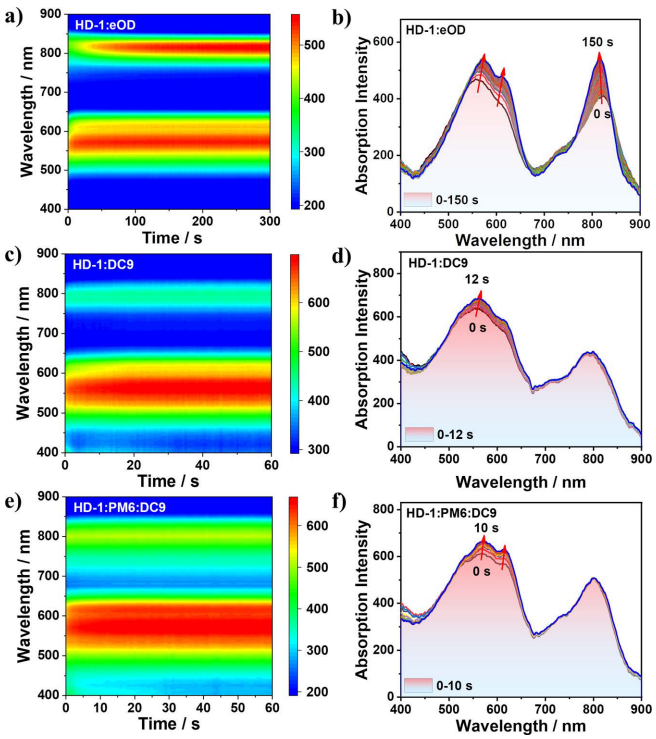

Figure 4 Absorption spectra of a—b) HD-1:eOD, c-d) HD-1:DC9, and e—f) HD-1:PM6:DC9 blend films during *in-situ* thermal annealing process at 140 °C, respectively.

restricted molecular aggregation and diffusion within the blend films. However, as depicted in Figure 5a, all devices maintained their PCEs above 98% of the initial values under continuous heating at 85 °C for 1000 h.

Subsequently, the AFM images of the HD-1:eOD, HD-1:DC9, and HD-1:PM6:DC9 blend films annealed at 85 °C after 500 and 1000 h were captured and are depicted in Figures 5b—5c, respectively. Notably, no significant phase separation or molecular self-aggregation was observed in any of the blend films following prolonged thermal annealing at 85 °C. Moreover, the slight increase in surface roughness observed across the three blend films during thermal aging could be neglected. Even after annealing at 85 °C for 1000 h, the HD-1:eOD, HD-1:DC9, and HD-1:PM6:DC9 blend films maintained uniform and smooth, active layer morphologies, suggesting that these systems possessed morphologies approaching thermodynamic stability during thermal aging. This characteristic is conducive to the long-term stable operations of the corresponding blend films.

Furthermore, the molecular stacking and crystallization behaviors of the three blend films after thermal aging at 85 °C were examined based on GIWAXS analysis. As depicted in Figures 6a—6b, after 200 and 1000 h of thermal aging, all HD-1-based blend films exhibited similar diffraction patterns, featuring distinct (010) and (100) diffraction peaks along the OOP and IP directions, respectively. This indicates that the desired face-on molecular orientations of the films were largely retained even after extended periods of thermal aging. Moreover, as summarized in Table S5 (Figure S5) and illustrated in Figured 6c—6d, following 200 and 1000 h of thermal aging at 85 °C, the stacking distance and CL values in the (010) and (100) regions of the HD-1:eOD and HD-1:DC9 blend films exhibited no significant changes, suggesting the formation and retention of a thermodynamically stable state in the HD-1-based blend films following post thermal annealing. Conversely, the HD-1:PM6:DC9 ternary film exhibited a slight decrease in $d_{\pi-\pi}$ from 3.79 Å to 3.75 Å, along with an increase in its CL value from 20.9 Å to 22.3 Å, indicating a tendency toward slightly increased crystallinity. This result may be attributed to the relatively looser packing scheme and the longer conjugated backbone of PM6 compared to those of HD-1, leading to more gradual molecular movements and rearrangements in the ternary blends during thermal aging. Despite these minor changes in the ternary blend films, their appropriate phase separation behaviors and enhanced molecular packing patterns contributed to sustained device performance.

These findings indicate that blend films based on the SMD HD-1 demonstrate excellent thermally stable morphologies, regardless of the types of acceptors used (monomeric or dimeric) or combinations with polymer materials. Additionally, the high crystallinities of the SMD and acceptor HD-1 and eOD, respectively, are seemingly crucial for realizing thermodynamically stable morphologies in ASM blend films.

Conclusions

To examine the morphological stabilities of the active layers in ASM-OSCs, a dimerized acceptor molecule, DC9, was synthesized from a 2-octyl-dodecyl-substituted small-molecule acceptor, eOD. While this dimeric acceptor molecule increased the T_g values of materials, its planarity and crystallinity deteriorated. The all-small molecule blend utilizing HD-1:eOD demonstrated a PCE of 15.13%, surpassing the corresponding value of 14.10% for the HD-1:DC9 blend. This lower efficiency of the HD-1:DC9 blend can be attributed to restricted molecular movements of DC9 molecules during thermal annealing, leading to poor intermolecular stacking patterns and challenges in controlling active layer morphologies. While, incorporating the polymer donor PM6 into the HD-1:DC9 blend improved its morphology and charge transport dynamics, resulting in a device efficiency of over 16%. Remarkably, morphological characterization results further affirmed that the surface morphologies and molecular packing behaviors of the blend films

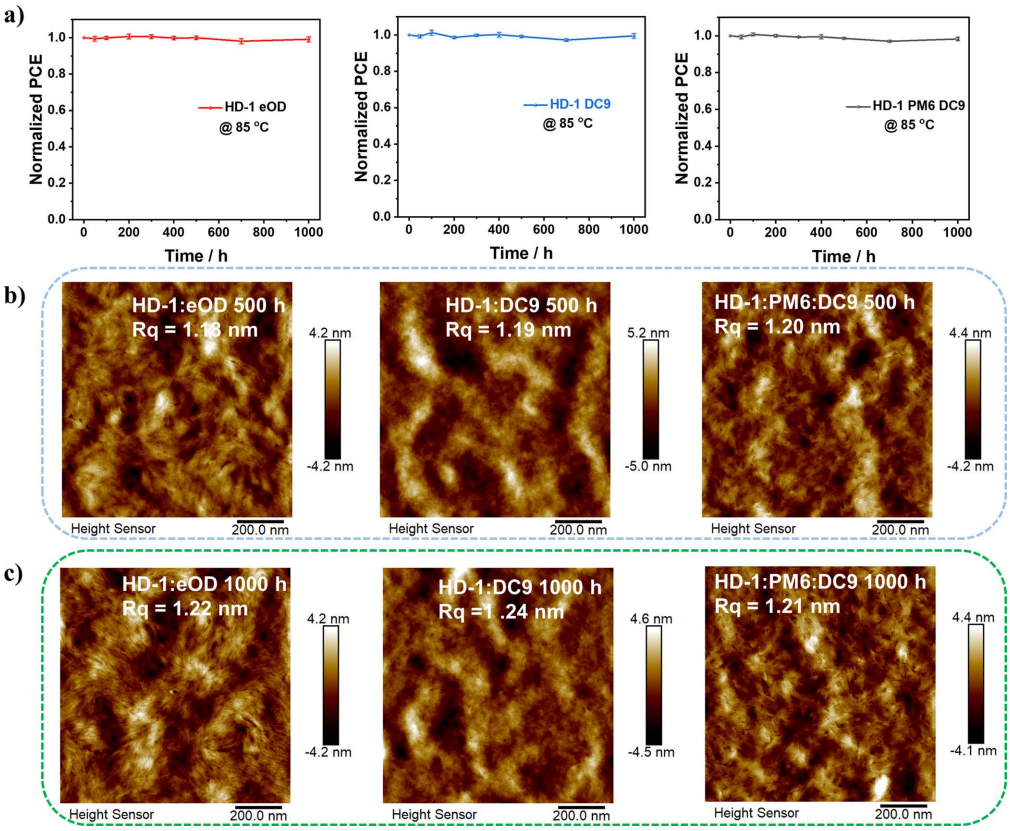

Figure 5 a) Device thermal stability under continuous heating conditions of 85 °C based on HD-1:eOD, HD-1:DC9, and HD-1:PM6:DC9 blend films. AFM images of the thermal aged blend films based on HD-1:eOD, HD-1:DC9 and HD-1:PM6:DC9 annealed at 85 °C for a) 500 h, and c) 1000 h, respectively.

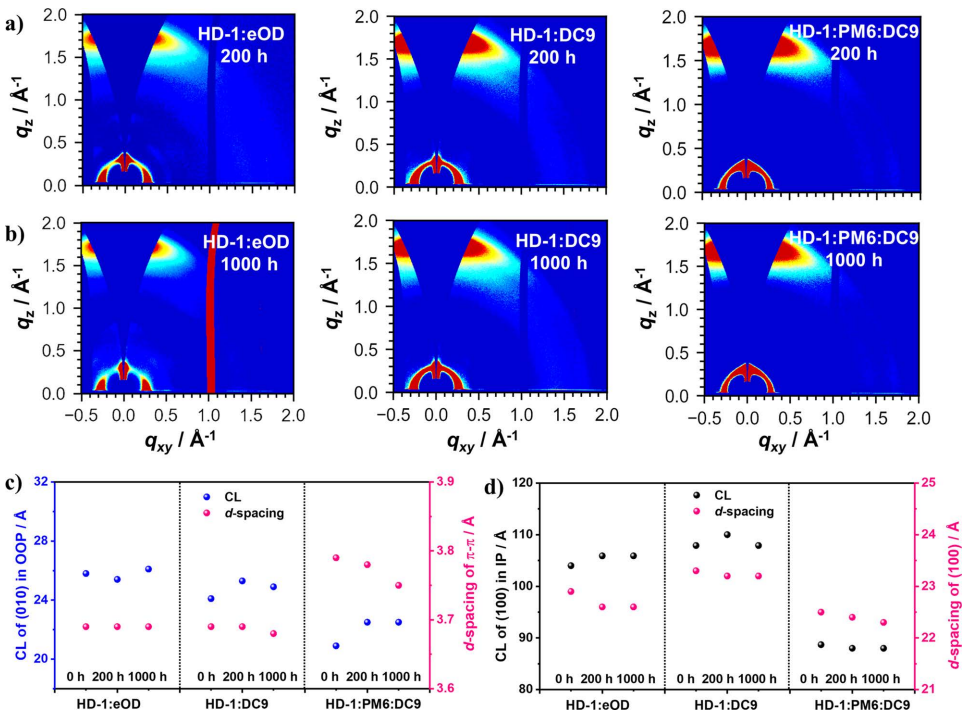

Figure 6 GIWAXS patterns of the thermal aged blend films based on HD-1:eOD, HD-1:DC9, and HD-1:PM6:DC9 annealed at 85 °C for a) 200 h, and b) 1000 h, respectively. The stacking distances and crystal coherence length corresponding to c) (010) scattering peak, and d) (100) scattering peak, respectively.

based on HD-1 were largely retained even after prolonged annealing and aging at 85 °C. Consequently, the PCEs of the blend films based on HD-1:eOD, HD-1:DC9, and HD-1:PM6:DC9 consistently remained above 98% of their initial efficiency even after 1000 h of thermal annealing aging at 85 °C. This indicates that the fabricated SMD-based active layers exhibit excellent thermal stability, with no significant changes in relation to the T_g values of their acceptor molecules. These findings contribute to our understanding of the thermal stabilities of ASM active layers and are anticipated to advance the development of ASM-OSCs.

Experimental

All the experimental details are provided in Supporting information.

Supporting Information

The supporting information for this article is available on the WWW under https://doi.org/10.1002/cjoc.202400573.

Acknowledgement

The authors gratefully acknowledge the financial support from MoST of China (2022YFB4200400, 2019YFA0705900, and 2023YFE0210400), NSFC (52303237, 21935007, 52025033, 52373189, and 22361132530). The authors thank the Beijing Synchrotron Radiation Facility, Institute of High Energy Physics for performing GIWAXS measurements.

References

[1] (a) Zhang, Q.; Kan, B.; Liu, F.; Long, G.; Wan, X.; Chen, X.; Zuo, Y.; Ni, W.; Zhang, H.; Li, M.; Hu, Z.; Huang, F.; Cao, Y.; Liang, Z.; Zhang, M.; Russell, T. P.; Chen, Y. Small-molecule solar cells with efficiency over 9%. *Nat. Photonics* **2015**, *9*, 35–41; (b) Huo, Y.; Zhang, H.-L.; Zhan, X. Nonfullerene All-Small-Molecule Organic Solar Cells. *ACS Energy Lett.* **2019**, *4*, 1241–1250; (c) Kan, B.; Kan, Y.; Zuo, L.; Shi, X.; Gao, K. Recent progress on all-small molecule organic solar cells using small-molecule nonfullerene acceptors. *InfoMat* **2021**, *3*, 175–200; (d) Tang, H.; Yan, C.; Huang, J.; Kan, Z.; Xiao, Z.; Sun, K.; Li, G.; Lu, S. Benzodithiophene-Based Small-Molecule Donors for Next-Generation All-Small-Molecule Organic Photovoltaics. *Matter* **2020**, *3*, 1403–1432.

[2] (a) Zhang, L.; Deng, D.; Lu, K.; Wei, Z. Optimization of Charge Management And Energy Loss in All-Small-Molecule Organic Solar Cells. *Adv. Mater.* **2024**, *36*, 2302915; (b) Chen, Y.; Wan, X.; Long, G. High Performance Photovoltaic Applications Using Solution-Processed Small Molecules. *Acc. Chem. Res.* **2013**, *46*, 2645–2655; (c) Ge, J.; Xie, L.; Peng, R.; Ge, Z. Organic Photovoltaics Utilizing Small-Molecule Donors and Y-series Nonfullerene Acceptors. *Adv. Mater.* **2023**, *35*, 2206566; (d) Wan, X.; Li, C.; Zhang, M.; Chen, Y. Acceptor-donor-acceptor type molecules for high performance organic photovoltaics - chemistry and mechanism. *Chem. Soc. Rev.* **2020**, *49*, 2828–2842; (e) Mishra, A. Material Perceptions and Advances in Molecular Heteroacenes for Organic Solar Cells. *Energy Environ. Sci.* **2020**, *13*, 4738; (f) Mishra, A.; Sharma, G. D. Harnessing the Structure-Performance Relationships in Designing Non-Fused Ring Acceptors for Organic Solar Cells. *Angew. Chem. Int. Ed.* **2023**, *62*, e202219245; (g) Zhang, G.; Zhao, J.; Chow, P. C. Y.; Jiang, K.; Zhang, J.; Zhu, Z.; Zhang, J.; Huang, F.; Yan, H. Nonfullerene Acceptor Molecules for Bulk Heterojunction Organic Solar Cells. *Chem. Rev.* **2018**, *118*, 3447; (h) Zhang, J.; Tan, H. S.; Guo, X.; Facchetti, A.; Yan, H. Material Insights and Challenges for Non-fullerene Organic Solar Cells Based on Small Molecular Acceptors. *Nat. Energy* **2018**, *3*, 720.

[3] (a) Yuan, J.; Zhang, Y.; Zhou, L.; Zhang, G.; Yip, H.-L.; Lau, T.-K.; Lu, X.; Zhu, C.; Peng, H.; Johnson, P. A.; Leclerc, M.; Cao, Y.; Ulanski, J.; Li, Y.; Zou, Y. Single-Junction Organic Solar Cell with over 15% Efficiency Using Fused-Ring Acceptor with Electron-Deficient Core. *Joule* **2019**, *3*, 1140–1151; (b) Li, C.; Zhou, J.; Song, J.; Xu, J.; Zhang, H.; Zhang, X.; Guo, J.; Zhu, L.; Wei, D.; Han, G.; Min, J.; Zhang, Y.; Xie, Z.; Yi, Y.; Yan, H.; Gao, F.; Liu, F.; Sun, Y. Non-fullerene acceptors with branched side chains and improved molecular packing to exceed 18% efficiency in organic solar cells. *Nat. Energy* **2021**, *6*, 605–613; (c) Chen, H.; Zou, Y.; Liang, H.; He, T.; Xu, X.; Zhang, Y.; Ma, Z.; Wang, J.; Zhang, M.; Li, Q.; Li, C.; Long, G.; Wan, X.; Yao, Z.; Chen, Y. Lowing the energy loss of organic solar cells by molecular packing engineering via multiple molecular conjugation extension. *Sci. China Chem.* **2022**, *65*,

1362–1373; (d) Cui, Y.; Yao, H.; Zhang, J.; Xian, K.; Zhang, T.; Hong, L.; Wang, Y.; Xu, Y.; Ma, K.; An, C.; He, C.; Wei, Z.; Gao, F.; Hou, J. Single-Junction Organic Photovoltaic Cells with Approaching 18% Efficiency. *Adv. Mater.* **2020**, *32*, 1908205.

[4] (a) Zhang, L.; Zhu, X.; Deng, D.; Wang, Z.; Zhang, Z.; Li, Y.; Zhang, J.; Lv, K.; Liu, L.; Zhang, X.; Zhou, H.; Ade, H.; Wei, Z. High Miscibility Compatible with Ordered Molecular Packing Enables an Excellent Efficiency of 16.2% in All-small-molecule Organic Solar Cells. *Adv. Mater.* **2022**, *34*, 2106316; (b) Wu, S.; Feng, W.; Meng, L.; Zhang, Z.; Si, X.; Chen, Y.; Wan, X.; Li, C.; Yao, Z.; Chen, Y. 15.51% efficiency all-small-molecule organic solar cells achieved by symmetric thiazolyl substitution. *Nano Energy* **2022**, *103,* 107801; (c) Duan, T.; Chen, Q.; Yang, Q.; Hu, D.; Cai, G.; Lu, X.; Lv, J.; Song, H.; Zhong, C.; Liu, F.; Yu, D.; Lu, S. Simple thiazole-centered oligothiophene donor enables 15.4% efficiency all small molecule organic solar cells. *J. Mater. Chem. A* **2022**, *10*, 3009–3017; (d) Qin, J.; An, C.; Zhang, J.; Ma, K.; Yang, Y.; Zhang, T.; Li, S.; Xian, K.; Cui, Y.; Tang, Y.; Ma, W.; Yao, H.; Zhang, S.; Xu, B.; He, C.; Hou, J. 15.3% efficiency all-small-molecule organic solar cells enabled by symmetric phenyl substitution. *Sci. China Mater.* **2020**, *63*, 1142–1150.

[5] (a) Feng, W.; Ma, K.; Song, G.; Shao, T.; Liang, H.; Lu, S.; Chen, Y.; Long, G.; Li, C.; Wan, X.; Yao, Z.; Kan, B.; Chen, Y. P-doped all-small-molecule organic solar cells with power conversion efficiency of 17.73%. *Sci. China Chem.* **2023**, *66*, 2371–2379; (b) Sun, Y.; Nian, L.; Kan, Y.; Ren, Y.; Chen, Z.; Zhu, L.; Zhang, M.; Yin, H.; Xu, H.; Li, J.; Hao, X.; Liu, F.; Gao, K.; Li, Y. Rational control of sequential morphology evolution and vertical distribution toward 17.18% efficiency all-small-molecule organic solar cells. *Joule* **2022**, *6*, 2835–2848; (c) Zhang, L.; Sun, R.; Zhang, Z.; Zhang, J.; Zhu, Q.; Ma, W.; Min, J.; Wei, Z.; Deng, D. Donor End-capped Alkyl Chain Length Dependent Non-Radiative Energy Loss in All-small-molecule Organic Solar Cells. *Adv. Mater.* **2022**, *34*, 2207020; (d) Gao, Y.; Yang, X.; Wang, W.; Sun, R.; Cui, J.; Fu, Y.; Li, K.; Zhang, M.; Liu, C.; Zhu, H.; Lu, X.; Min, J. High-Performance Small Molecule Organic Solar Cells Enabled by a Symmetric-Asymmetric Alloy Acceptor with a Broad Composition Tolerance. *Adv. Mater.* **2023**, *35*, 2300531.

[6] Burlingame, Q.; Ball, M.; Loo, Y. L. It's time to focus on organic solar cell stability. *Nat. Energy* **2020**, *5*, 947–949.

[7] Luponosov, Y. N.; Solodukhin, A. N.; Mannanov, A. L.; Trukhanov, V. A.; Peregudova, S. M.; Pisarev, S. A.; Bakirov, A. V.; Shcherbina, M. A.; Chvalun, S. N.; Paraschuk, D. Y.; Ponomarenko, S. A. Highly soluble and thermally stable alkyl-free star-shaped D-π-A oligomer with electron-withdrawing phenyldicyanovinyl groups for organic photovoltaics. *Org. Electron.* **2017**, *51*, 180–189.

[8] Sun, R.; Wu, Y.; Guo, J.; Wang, Y.; Qin, F.; Shen, B.; Li, D.; Wang, T.; Li, Y.; Zhou, Y.; Lu, G.; Li, Y.; Min, J. High-performance all-small-molecule organic solar cells without interlayers. *Energy Environ. Sci.* **2021**, *14*, 3174–3183.

[9] (a) Chen, H.; Cao, X.; Xu, X.; Li, C.; Wan, X.; Yao, Z.; Chen, Y. A Low Reorganization Energy and Two-dimensional Acceptor with Four End Units for Organic Solar Cells with Low Eloss. *Chinese J. Polym. Sci.* **2022**, *40*, 921–927; (b) Li, S.; Zhang, R.; Zhang, M.; Yao, J.; Peng, Z.; Chen, Q.; Zhang, C.; Chang, B.; Bai, Y.; Fu, H.; Ouyang, Y.; Zhang, C.; Steele, J. A.; Alshahrani, T.; Roeffaers, M. B. J.; Solano, E.; Meng, L.; Gao, F.; Li, Y.; Zhang, Z.-G. Tethered Small-Molecule Acceptors Simultaneously Enhance the Efficiency and Stability of Polymer Solar Cells. *Adv. Mater.* **2023**, *35*, 2206563; (c) Liang, Y.; Zhang, D.; Wu, Z.; Jia, T.; Lüer, L.; Tang, H.; Hong, L.; Zhang, J.; Zhang, K.; Brabec, C. J.; Li, N.; Huang, F. Organic solar cells using oligomer acceptors for improved stability and efficiency. *Nat. Energy* **2022**, *7*, 1180–1190.

[10] Nakano, K.; Chen, Y.; Xiao, B.; Han, W.; Huang, J.; Yoshida, H.; Zhou, E.; Tajima, K. Anatomy of the energetic driving force for charge generation in organic solar cells. *Nat. Commun.* **2019**, *10*, 2520.

[11] (a) Ghasemi, M.; Balar, N.; Peng, Z.; Hu, H.; Qin, Y.; Kim, T.; Rech, J. J.; Bidwell, M.; Mask, W.; McCulloch, I.; You, W.; Amassian, A.; Risko, C.; O'Connor, B. T.; Ade, H. A molecular interaction–diffusion framework for predicting organic solar cell stability. *Nat. Mater.* **2021**, *20*, 525–532; (b) Root, S. E.; Alkhadra, M. A.; Rodriquez, D.; Printz, A. D.; Lipomi, D. J. Measuring the Glass Transition Temperature of Conjugated Polymer Films with Ultraviolet–Visible Spectroscopy. *Chem. Mater.* **2017**, *29*, 2646–2654.

[12] Koster, L. J. A.; Mihailetchi, V. D.; Ramaker, R., Blom, P. W. M. Light intensity dependence of open-circuit voltage of polymer:fullerene solar cells. *Appl. Phys. Lett.* **2005**, *86*, 123509.

[13] Kyaw, A. K. K.; Wang, D. H.; Gupta, V.; Leong, W. L.; Ke, L.; Bazan, G. C.; Heeger, A. J. Intensity Dependence of Current–Voltage Characteristics and Recombination in High-Efficiency Solution-Processed Small-Molecule Solar Cells. *ACS Nano* **2013**, *7*, 4569–4577.

[14] Shockley, W.; Queisser, H. J. Detailed Balance Limit of Efficiency of p-n Junction Solar Cells. *J. Appl. Phys.* **1961**, *32*, 510–519.

[15] Wang, Y.; Qian, D.; Cui, Y.; Zhang, H.; Hou, J.; Vandewal, K.; Kirchartz, T.; Gao, F. Optical Gaps of Organic Solar Cells as a Reference for Comparing Voltage Losses. *Adv. Energy Mater.* **2018**, *8*, 1801352.

[16] Rau, U. Reciprocity relation between photovoltaic quantum efficiency and electroluminescent emission of solar cells. *Phys. Rev. B* **2007**, *76*, 085303.

[17] Rivnay, J.; Mannsfeld, S. C.; Miller, C. E.; Salleo, A.; Toney, M. F. Quantitative determination of organic semiconductor microstructure from the molecular to device scale. *Chem. Rev.* **2012**, *112*, 5488–5519.

[18] (a) Feng, W.; Chen, T.; Li, Y., Duan, T., Jiang, X.; Zhong, C.; Zhang, Y.; Yu, J.; Lu, G.; Wan, X.; Kan, B.; Chen, Y. Binary All-polymer Solar Cells with a Perhalogenated-Thiophene-Based Solid Additive Surpass 18% Efficiency. *Angew. Chem. Int. Ed.* **2024**, *63*, e202316698; (b) Song, J.; Zhang, C.; Li, C.; Qiao, J.; Yu, J.; Gao, J.; Wang, X.; Hao, X.; Tang, Z.; Lu, G.; Yang, R.; Yan, H.; Sun, Y. Non-halogenated Solvent-Processed Organic Solar Cells with Approaching 20 % Efficiency and Improved Photostability. *Angew. Chem. Int. Ed.* **2024**, *63*, e202404297.

Manuscript received: May 30, 2024
Manuscript revised: July 5, 2024
Manuscript accepted: July 11, 2024
Version of record online: XXXX, 2024

The Authors

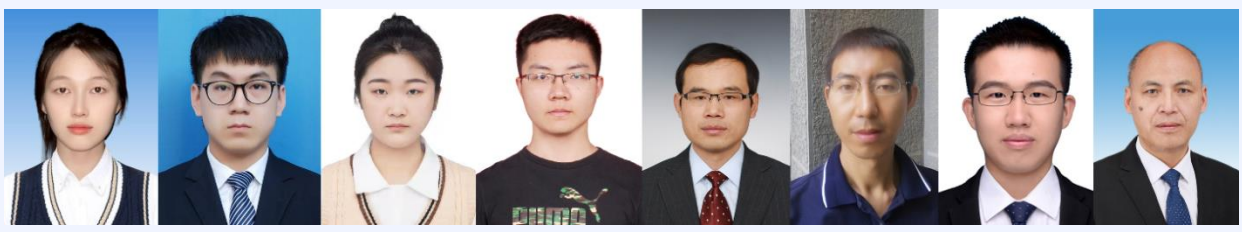

Left to Right: Wanying Feng, Yuyang Bai, Jiaying Wang, Shaohui Yuan, Xiangjian Wan, Yu Chen, Bin Kan, Yongsheng Chen

